Supercontinuum generation in high-index doped silica photonic integrated circuits under diverse pumping settings

C. KHALLOUF,[1] **V. T. HOANG,[2]** **G. FANJOUX,[1]** **B. LITTLE,[3]** **S. T. CHU,[4]** **D. J. MOSS,[5]** **R. MORANDOTTI,[6]** **J. M. DUDLEY,[1]** **B. WETZEL,[2]** AND **T. SYLVESTRE[1],***

[1]*Institut FEMTO-ST, CNRS-Université de Franche-Comté, 25030 Besançon, France*
[2]*XLIM Research Institute, CNRS UMR 7252, Université de Limoges, 87060 Limoges, France*
[3]*QXP Technologies Inc., Xi'an, China*
[4]*Department of Physics, City University of Hong Kong, Tat Chee Avenue, Hong Kong SAR, China*
[5]*Optical Sciences Centre, Swinburne University of Technology, Hawthorn, Victoria, Australia*
[6]*INRS-EMT, 1650 Boulevard Lionel-Boulet, Varennes, J3X 1S2 Québec, Canada*
*thibaut.sylvestre@univ-fcomte.fr

Abstract: Recent advances in supercontinuum light generation have been remarkable, particularly in the context of highly nonlinear photonic integrated waveguides. In this study, we thoroughly investigate supercontinuum (SC) generation in high-index doped silica glass integrated waveguides, exploring various femtosecond pumping wavelengths and input polarization states. We demonstrate broadband SC generation spanning from 700 nm to 2400 nm when pumping within the anomalous dispersion regime at 1200 nm, 1300 nm, and 1550 nm. In contrast, pumping within the normal dispersion regime at 1000 nm results in narrower SC spectra, primarily due to coherent nonlinear effects such as self-phase modulation and optical wave breaking, and also dispersive wave generation in the anomalous dispersion regime. We further examine the impact of both TE and TM polarization modes on SC generation, shedding light on the polarization-dependent characteristics of the broadening process. Additionally, we report the observation of two new Raman peaks at 48.8 THz and 75.1 THz in high-index glass using a confocal Raman micro-spectrometer. Incorporating these two peaks in the Raman gain modeling, we achieved good agreement between numerical simulations based on the modified nonlinear Schrödinger equation and experimental results. Finally, we present relative intensity noise measurements of the supercontinuum generated at 1550 nm using the real-time dispersive Fourier transform technique.

1. Introduction

Due to their unique combination of high brightness, multi-octave bandwidth, and fiber delivery, supercontinuum (SC) laser sources have revolutionized many applications, including optical coherence tomography (OCT), fluorescence imaging, optical sensing, absorption spectroscopy, and optical frequency comb metrology [1–9]. While SC light has been extensively researched and developed in optical fibers for over three decades, achieving record bandwidths spanning from the ultraviolet (UV) to mid-infrared (MIR) wavelength ranges, current efforts have shifted towards developing compact, low-threshold SC sources based on photonic integrated circuits (PICs). Recent technological advances in the design and fabrication of low-loss highly nonlinear integrated photonic chip waveguides are currently driving new research on SC generation in various materials, and yet unexplored regions of the electromagnetic spectrum such as the

mid-infrared. SC generation has already been investigated in many integrated and dispersion-engineered photonic integrated circuits based on a range of nonlinear materials, glasses or wide band-gap semiconductors, including silica (SiO_2) [10], doped silica (SiON) [11], silicon (Si) [12], silicon nitride (Si_3N_4) [13–15], silicon germanium (SiGe) [16,17], titanium dioxide (TiO_2) [18], chalcogenide glass (As_2S_3) [19], lithium niobate on insulator (LNOI) [20], Aluminum nitride (AiN) [21], and more recently Gallium arsenide (GaAs) [22]. For a comprehensive review of the recent progress on chip-based SC sources, we can refer to Ref. [23]. Among available nonlinear materials, highly-doped silica glass (HDSG) is quite promising as it possesses several advantages including both CMOS and silica fiber compatibility, a wide transparency window from 0.3 μm to 3 μm, a nonlinearity greater than pure fused silica, no free carrier or nonlinear absorption [11,24]. Although SC generation in a such waveguide has already been investigated in the past, the role of stimulated Raman scattering (SRS), various pumping and dispersion regimes, and polarization effects on SC generation hitherto remains elusive.

In this paper, we present a comprehensive experimental and numerical investigation of supercontinuum (SC) generation in nonlinear photonic integrated waveguides fabricated from highly-doped silica glass (HDSG) by QXP Technologies. The study focuses on both short (3 cm) and long (50 cm) spiral waveguides. We begin by introducing the QXP chip waveguides, describing their dimensions, refractive indices, and linear loss measurements at 1550 nm. Numerical calculations based on the waveguide cross-section are presented, including the effective refractive indices of the TE and TM fundamental modes, along with dispersion and nonlinearity parameters. Using a confocal Raman micro-spectrometer, we measured the Raman gain spectrum of HDSG, identifying new Raman peaks that are distinct from those of pure fused silica. We then investigated SC generation across a broad range of pumping wavelengths and dispersion regimes using a widely tunable femtosecond optical parametric oscillator. The experimental results are supported by numerical simulations based on a generalized nonlinear Schrödinger equation (GNLSE) that incorporates the updated Raman gain spectrum. Additionally, we investigated the polarization dependence of SC generation at 1550 nm and 1200 nm. Finally, relative intensity noise (RIN) measurements performed using the dispersive Fourier transform (DFT) technique confirm the excellent stability of SC spectra generated at 1550 nm [25].

2.   High-index doped silica chip waveguide

Since the early developments of high-index, low-loss, CMOS-compatible doped silica glass for applications to all-optical signal processing, significant progress has been made, achieving large-scale low-loss in highly-doped silica glass waveguides. Figure 1(a) shows the cross-section of the doped silica waveguide manufactured by QXP Technologies Inc. The core size is 1.5 $\mu m \times 1.52\,\mu m$, integrated into plasma-enhanced chemical vapor deposition (PECVD) silica (SiO_2), and deposited on SiO_2 thermal oxide, all on a silicon wafer. The chip core has a high refractive index $n = 1.7$ at 1550 nm. The chip comprises 20 reversible input/output waveguides, couplers, and delay lines, each connected to 25 cm-long fiber pigtails, facilitating the coupling and extraction of guided light. In our experiments, we investigated SC generation in a 50-cm-long HDSG waveguide, which includes two 25-cm-long spirals. We also compared with the results obtained in a shorter 3-cm long waveguide. The total insertion loss of the long (short) waveguide was measured to be 8.9 dB (3 dB) at 1550 nm using a high-resolution optical time domain reflectometer (OBR 4600 Luna Tech.). The OBR trace of the 50 cm-long waveguide is shown in Fig. 1(b) with a sampling resolution of 20 μm, and the linear loss was estimated to be as low as 0.1 dB.cm^{-1} [26].
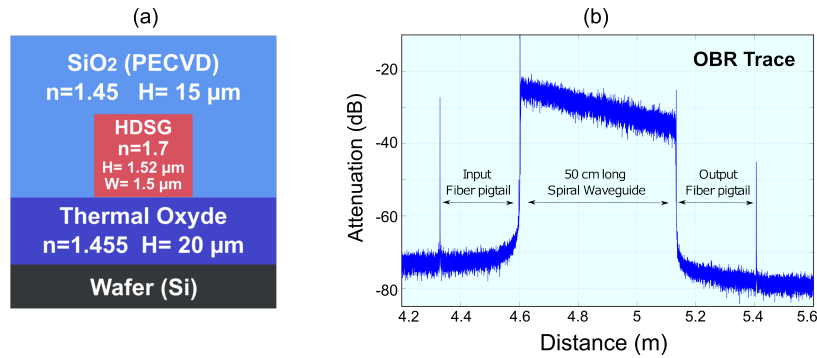
Fig. 1. (a) Cross-section of the highly doped silica glass waveguide (HDSG) from QXP technologies; (b): Attenuation trace showing the losses of the 50-cm long waveguide and the fiber pigtails at λ=1550 nm.

3. Dispersion and effective modal area

Based on the cross-section of the integrated waveguide shown in Fig. 1(a), we numerically calculated the effective refractive indices of the TE/TM fundamental modes, as well as the various dispersion and nonlinearity parameters. A finite element method (FEM) based software (Ansys Lumerical mode solutions) was used to determine these parameters by scanning the wavelength from 700 nm to 3000 nm, the region of interest for SC generation. The results are provided in Fig. 2, which shows the group-velocity dispersion D in panel (a) and the effective mode area A_{eff} in panel (b) for the two TE/TM fundamental modes, represented in blue and red, respectively. The dispersion profiles for both TE/TM modes exhibit three zero-dispersion wavelengths (ZDW) near 1065 nm, 1800 nm, and 2300 nm. The birefringence of the waveguide was estimated to be below 10^{-4} at 1550 nm.
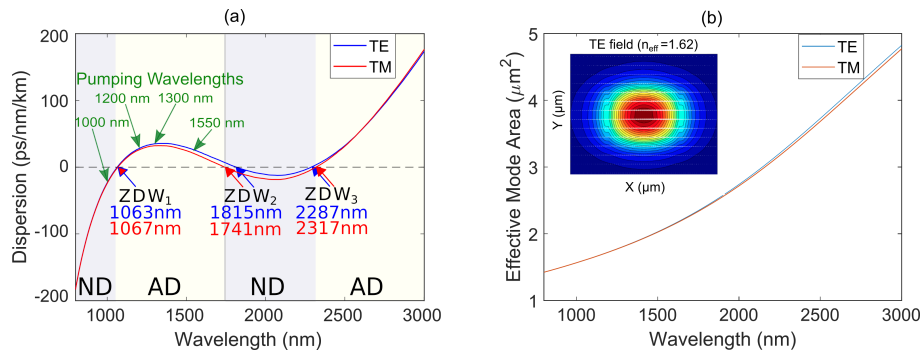
Fig. 2. (a): Group velocity dispersion D in ps/nm/km of the QXP-chip waveguide shown in Fig. 1 for the fundamental TE and TM modes in blue and red, respectively. ND and AD refer to normal and anomalous dispersion, respectively. Blue and red arrows indicate the three zero-dispersion wavelengths (ZDW) for each mode, respectively. Green arrows depict the pumping wavelengths considered experimentally. (b): Effective modal area A_{eff} of the two fundamental TE and TM modes versus wavelength. The inset shows the TE optical field transverse distribution.

According to Fig. 2, pumping wavelengths will cover both dispersion regimes from 1000 nm to 1550 nm. So when pumping at 1000 nm, i.e. in the normal dispersion regime, one can expect to get SC generation mediated by SPM and OWB, when pumping at 1200 nm, 1300 nm, 1550

nm, i.e. in the anomalous dispersion regime, one can expect to have a broader SC generated by high-order soliton fission, Raman-induced soliton self-frequency shift (SSFS), and dispersive wave (DW) emission. Figure 2(b) also demonstrates that the effective modal area A_{eff} of the two fundamental TE and TM modes strongly varies across wavelengths. This variation will impact the efficiency of SC generation and will be considered in the simulations.

## 4. Raman spectrum of the high-index doped silica glass

Before experimentally exploring SC generation, we first examined the Raman response of the high-index material using a high-resolution confocal Raman micro-spectrometer (Monovista CRS+). The Raman spectra presented in Fig. 3 were acquired by scanning from the top of the QXP chip waveguide, employing a 532 nm continuous doubled Nd:YAG laser beam and a 100x microscope objective. Achieving optimal depth focus was essential to ensure precise targeting of the laser beam onto the highly doped silica waveguide, rather than onto the surrounding silica coatings. The Raman spectra of silica (yellow) and silicon (orange) shown in Fig. 3 were obtained by focusing the laser beam onto the upper layer of the PECVD SiO_2 layer and the silicon wafer, respectively. During the focusing process on the doped silica material, Raman scattering from silica originating from the surrounding coatings, as well as from the material itself, along with signals from the silicon wafer, were consistently observed. However, notable is the emergence of two distinct peaks at 1627 cm^{-1} (48.8 THz) and 2504 cm^{-1} (75.1 THz), in addition to the usual silica peak at 450 cm^{-1} (13.2 THz). These two new Raman peaks originate from O_2 and N_2 molecular vibrational states, respectively [27]. This refined Raman gain profile, measured experimentally (in blue), will be further included in our simulations to improve the modeling of SC generation.

5. Experimental setup

The experimental setup used for generating and characterizing SC spectra is shown in Fig. 4. A 200-fs Optical Parametric Oscillator (OPO) served as the pump laser. It is driven by a Ti:Sapphire mode-locked laser (Coherent Chameleon Ultra II) at an 80 MHz repetition rate tunable from 680 to 1080 nm. The OPO signal is tunable within the range 1-1.6 μm with mean output powers from 230 mW to 1 W, and the idler from 1.7 μm to 4 μm with powers ranging from 250 mW to 50 mW. Control over power and polarization angles θ were achieved through a variable density filter and a half-wave plate, respectively. The OPO signal was then injected into an SMF-28 fiber pigtail with a 55% coupling efficiency using a 40x IR focusing objective mounted on a multi-axis fiber alignment stage. The light was fiber-coupled into the QXP chip waveguides using the input polarization-maintaining fiber pigtail, aligned with the TE/TM axis of the waveguide. The output-generated SC light was analyzed using two different spectrometers to cover the full SC bandwidth. An Agilent 86142B (OSA1) was used for the range 600-1700 nm, with a lower responsivity from 1700 to 2000 nm, and an FTIR Thorlabs (OSA2, model 205C) was used for the range of 1000-5600 nm. To complete the spectral measurements, we also analyzed the real-time SC stability and relative intensity noise (RIN) when pumping at 1550 nm using the dispersive Fourier transform (DFT) technique [25,28,29]. This technique utilized a 170-m long dispersion-compensating fiber (DCF) to stretch the pulses and measure the fluctuating pulse-to-pulse SC spectra in the time domain via a dispersive transformation. The output stretched pulses were detected with a high-speed 50-GHz high-power photodiode (FINISAR, model HPDV2120R) and recorded using a 20 GHz bandwidth real-time oscilloscope (Keysight Agilent DSA91204A, 20GHz, 40 GSa/s) [30].
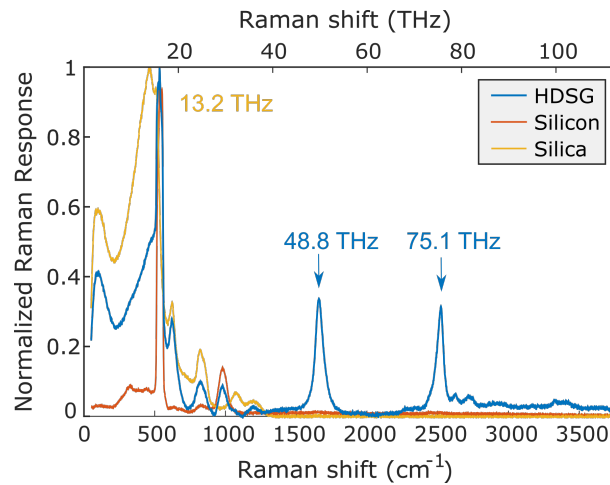
Fig. 3. Raman spectra of the integrated HDSG waveguide in blue, of the silicon in orange, and silica in yellow. A normalization was employed for clarity purposes in the presented data.
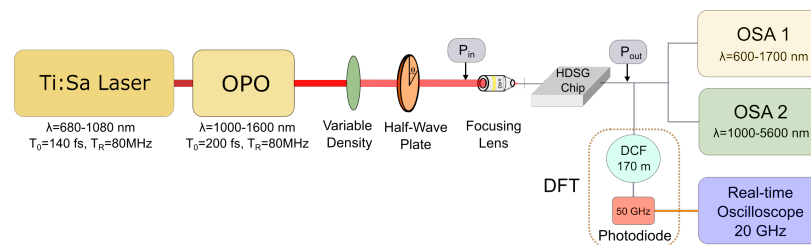

Fig. 4. Experimental setup for SC generation and characterization. Ti:Sa Laser: Titanium-Sapphire laser; OPO: Optical parametric oscillator; OSA: Optical spectrum analyzer; DCF: Dispersion compensating fiber. DFT: Dispersive Fourier transform.

6. Experimental SC results

Figure 5 shows the 50 cm long waveguide output SC spectra for three different pumping wavelengths (1550 nm, 1300 nm, 1200 nm) with increasing pump powers for each wavelength setting. As anticipated, the supercontinuum (SC) generated across these various pumping wavelengths arises from soliton self-frequency shift within the AD regime, coupled with dispersive wave generation transitioning into the ND regime. Notably, when employing a pump wavelength of 1550 nm, typical for telecom applications, the resulting SC spectrum spans from 700 nm to well beyond the upper limit of the Agilent analyzer (OSA1) at 2000 nm (Fig. 5(a)), so that extended measurements utilizing the Thorlabs OSA2 were necessary (see Fig. 5(b)). However, to prevent intensity saturation of the Thorlabs spectrometer, the input power at the entrance of the focusing objective was limited to 220 mW, corresponding to an output power of 10 mW. Despite this limited power, a discernible SC is evident, extending up to 2400 nm for a 220 mW input power. Figure 5(a) also shows a residual peak (- 40 dB compared to the pump) located at 1740 nm, which comes from the OPO idler rather than the waveguide. We verified that this weak signal neither contributes nor interferes with the SC generation process. For other pumping wavelengths at 1300 nm and 1200 nm, respectively, idler residues extend beyond 2000 nm and do not appear in the measurements. The SCs depicted in Figs. 5(c) and (d) span from 750 nm to 1800 nm. Here, the input polarization angle was chosen to maximize SC bandwidth,

suggesting compatibility with the TE or TM mode. The spectral dip observed at 1380 nm is due to residual water (OH^-) absorption which is still present within the integrated waveguide. Nonetheless, this absorption does not impede SC extension towards the infrared.

Figure 6 illustrates spectral broadening obtained when pumping at 1000 nm, within the ND regime and close to the first ZDW. As expected, a limited SC extension is observed, primarily attributed to self-phase modulation (SPM) and optical wave breaking (OWB) [31]. At lower power levels, the SC exhibits quasi-symmetric spectral broadening, ceasing upon reaching the first zero-dispersion wavelength (ZDW1) near 1065 nm when pumped at higher powers. Notably, a distinctive peak emerges near 1150 nm, characteristic of dispersive wave generation from SPM within the AD regime, a phenomenon previously observed in optical fibers [32]. This observation will be further corroborated through numerical simulations (See Fig. 9(d)).
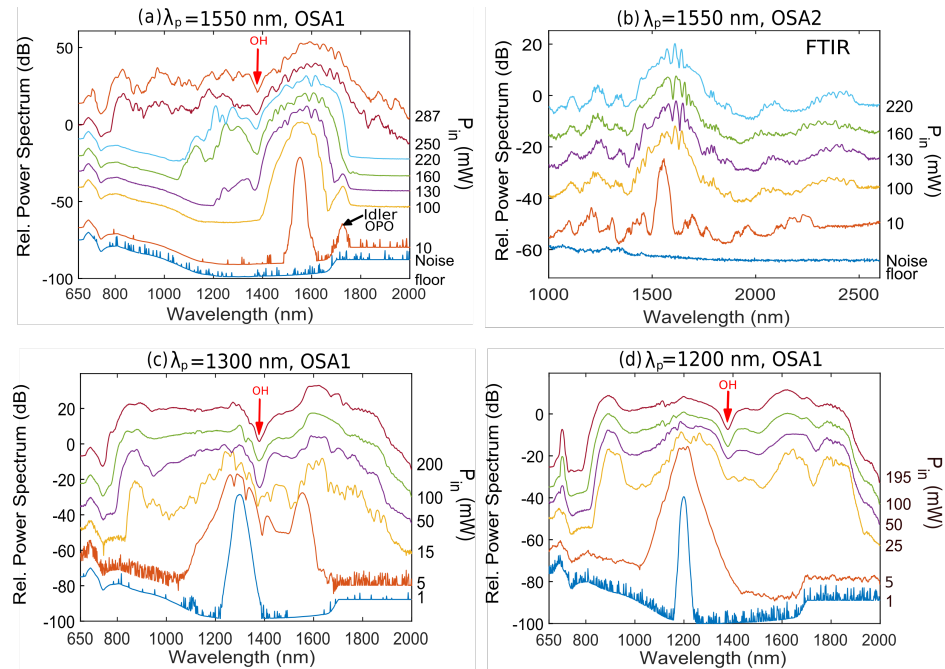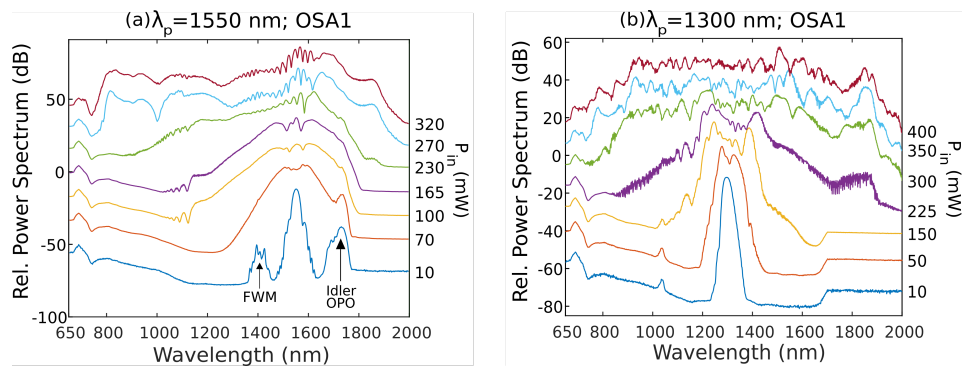

Fig. 5. SC spectra generated in the 50 cm waveguide in the anomalous dispersion pumping regime for an increasing input mean power measured at the entry of the focusing objective, shown on the right side of the graph for different pumping wavelengths λ_P (1550 nm, 1300 nm, and 1200 nm); (a),(c),(d) were measured with the Agilent OSA1 while (b) was measured with the Thorlabs OSA2. All spectra are vertically shifted for improved clarity.

In addition to the experiments reported on the 50 cm spiral waveguide, SC measurements were performed using a 3 cm high-index silica waveguide having the same cross-section. Figure 7(a) and (b) show the output SC spectra when pumping at 1550 nm and 1300 nm, respectively, with increasing input mean pump power up to 400 mW. Despite the shorter waveguide, the SC still extends from approximately 800 nm to 1900 nm with good flatness. This indicates that the femtosecond SC is mainly generated while propagating in the first few centimeters of the chip waveguide. Consequently, careful design considerations are essential for optimizing SC bandwidth and output power in on-chip SC generation.
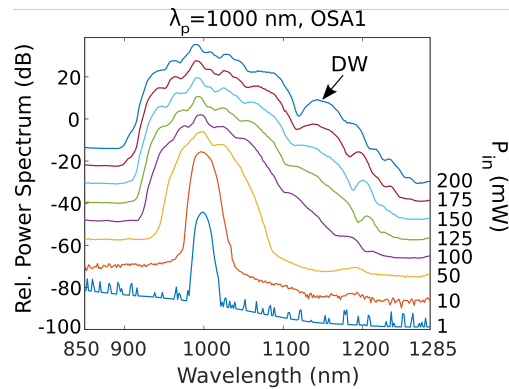
Fig. 6. SC spectra generated in the 50 cm waveguide in the normal dispersion regime with increasing average input power, shown on the right side of the graph, when pumping at 1000 nm, measured with the Agilent OSA1. The DW generated through SPM in the anomalous dispersion regime is marked by an arrow.

Fig. 7. SC spectra generated in the 3 cm waveguide in the anomalous dispersion regime with increasing input power, shown on the right side of the graph when pumping at (a): 1550 nm and (b): 1300 nm measured with the Agilent OSA1.

7. Polarization analysis

Next, we investigated the SC variations by rotating the input polarization angle relative to the waveguide's TE/TM axes. When pumping at 1550 nm, Fig. 8(a) shows a notable dependency of the SC generation process on the polarization angle. The SC exhibits a wide spectral spread ranging from 800 nm to 2000 nm for specific polarization angles, whereas, for others, it spans over a reduced spectral range from 1150 nm to 1800 nm. This reduced SC efficiency can be easily attributed to pulse broadening due to polarization mode dispersion when the input polarization is not aligned with one of the principal axes of the waveguide. As expected, there is an observed angle periodicity of approximately 90°. For instance, SC spectra exhibit similar characteristics at polarization angles of 60°, 160°, and 240° (see bold lines in Fig. 8(a)). Conversely, when pumping at 1200 nm, as depicted in Fig. 8(b), the polarization angle demonstrates less influence on the SC generated within the 800-2000 nm range. This is mainly due to the small difference between the dispersion values at 1200 nm for the fundamental TE and TM modes, unlike for the pumping wavelength of 1550 nm where the difference is more important (See Fig. 2(a)). However, a distinct peak near 705 nm can be seen in Fig. 8(b), which displays strong polarization dependence with a periodicity of 180°. This peak has been identified from numerical simulations

as resulting from a phase-matched four-wave mixing (FWM) involving the pump at 1200 nm and the dispersive wave at 892 nm. We have checked that the phase-matching condition related to this FWM : $2\beta_{892nm} - \beta_{1200nm} - \beta_\lambda = 0$ is satisfied around $\lambda = 705$ nm.

8.   Numerical simulations

To model SC generation within the doped silica chip waveguides, we used the scalar generalized nonlinear Schrödinger equation (GNLSE), including the new Raman gain spectrum and the wavelength-dependent losses. This equation is expressed in the following reduced form [2]

$$\frac{\partial A}{\partial z} + \frac{\alpha(\omega)}{2}A - \sum_{n \geq 2} \frac{i^{n+1}}{n!}\beta_n \frac{\partial^n A(z,T)}{\partial T^n} = i\gamma(1 + i\tau_0 \frac{\partial}{\partial T})\left(A \int_{-\infty}^{\infty} R(T')|A(z,T-T')|^2 dT'\right), \quad (1)$$

where A(z,T) is the complex amplitude of the field propagating in the z direction and in the pump velocity time frame T. $\alpha(\omega)$ is the frequency-dependent propagation loss, β_n is the nth derivative of the propagation constants. The nonlinear coefficient $\gamma = 2\pi n_2/(\lambda_p A_{eff}(\lambda))$ is obtained from the nonlinear index of the high index silica glass $n_2 = 1.15 \times 10^{-19} m^2/W$ [33] and $A_{eff}(\lambda_p)$, the effective area of the fundamental mode [34]. The nonlinear coefficient was estimated from the computed modal area plotted in Fig. 2(b), yielding $\gamma = 250 \, W^{-1} km^{-1}$ at 1550 nm, which is approximately 200 times larger than a standard silica fiber (SMF-28). The temporal derivation of the field envelope on the right side of Eq. (1) corresponds to the self-steepening effect with its characteristic time scale $\tau_0 = 1/\omega_0$ (ω_0 being the input pulse angular frequency). $R(T) = (1 - f_R)\delta(T) + f_R h_R(T)$ is the global nonlinear response, where $h_R(T)$ is the delayed temporal Raman response, and f_R the fractional contribution of the Raman effect, which we assume as f_R=0.18, the value of fused silica [34]. We also consider in the numerical Raman model the new Raman gain curve shown in blue in Fig. 3), which includes the two new Raman peaks at 48.8 THZ and 75.1 THz. Including the two new peaks in the Raman gain modeling has been shown to slightly improve the fit to the experimental SC output spectra compared to the standard Raman gain curve for fused silica alone. However, their impact in the femtosecond pumping regime remains minimal, with only minor differences observed in SC bandwidth and flatness. The dominant effect still arises from the main silica peaks in this regime. The influence of these new peaks is expected to be more significant with longer pulse durations (ps or ns) or in continuous wave pumping, where Raman-induced soliton self-frequency shifts and cascaded stimulated Raman scattering are more prominent. As initial conditions, we consider Gaussian-shaped pulses with 200 fs duration (FWHM), and we also add quantum noise as one photon per mode with random phase as well as the relative intensity noise of the pump laser (1%), as in Ref. [35]. In our simulations, we averaged the results of 200 different pulses under varying input noise conditions, assuming a polarization vector aligned with either the fundamental TE or TM mode. Additionally, we take into account the spectral dip resulting from OH- absorption into the simulation as a Gaussian filter centered at 1380 nm. Finally, the simulations also considered nonlinear propagation in the short fiber pigtails before the integrated waveguide, assuming standard dispersion and nonlinear coefficients for single-mode fibers.

   Figures 9(a-d) present the simulated SC spectra for different input peak powers (P_0) while considering the same four pumping wavelengths (λ_P) used in the experiment. As can be seen, a quite good agreement is observed between these simulations and the experimental data shown in Figs. 5 and 6. Specifically, when pumping at 1550 nm, the simulated SC spreads from 700 nm to 2400 nm (Fig. 9(a)). Similarly, for a pump wavelength of 1300 nm, the simulated SC also extends from 750 nm to 2000 nm (Fig. 9(b)). The peak observed experimentally at 705 nm when pumping at 1200 nm is also replicated in the simulations, with the SC spanning from 700 nm to 2000 nm (Fig. 9(c)). This peak relies on a FWM interaction within the SC, as was discussed earlier.
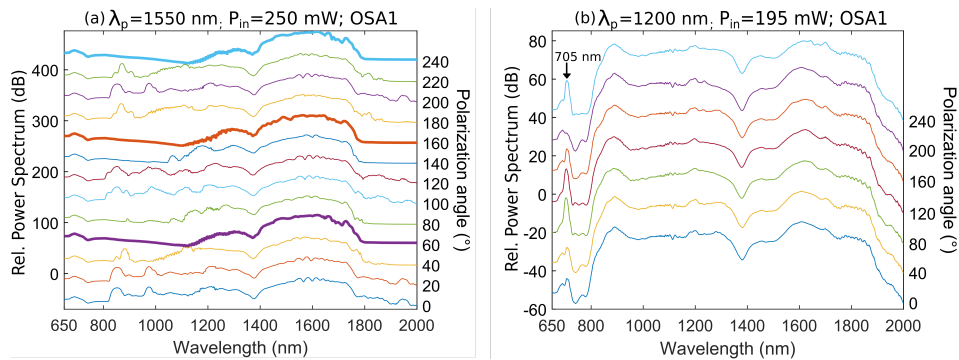
Fig. 8. SC generation in the anomalous dispersion regime for different input polarization angles, depicted on the right side of the graph with an input power P_{in} measured at the entry of the focusing objective for a pumping wavelength of (a) 1550 nm with P_{in}= 250 mW ; (b) 1200 nm with P_{in}= 195 mW. The 90° periodicity of the input polarization angle is illustrated by bold lines for the corresponding SC spectra in (a).
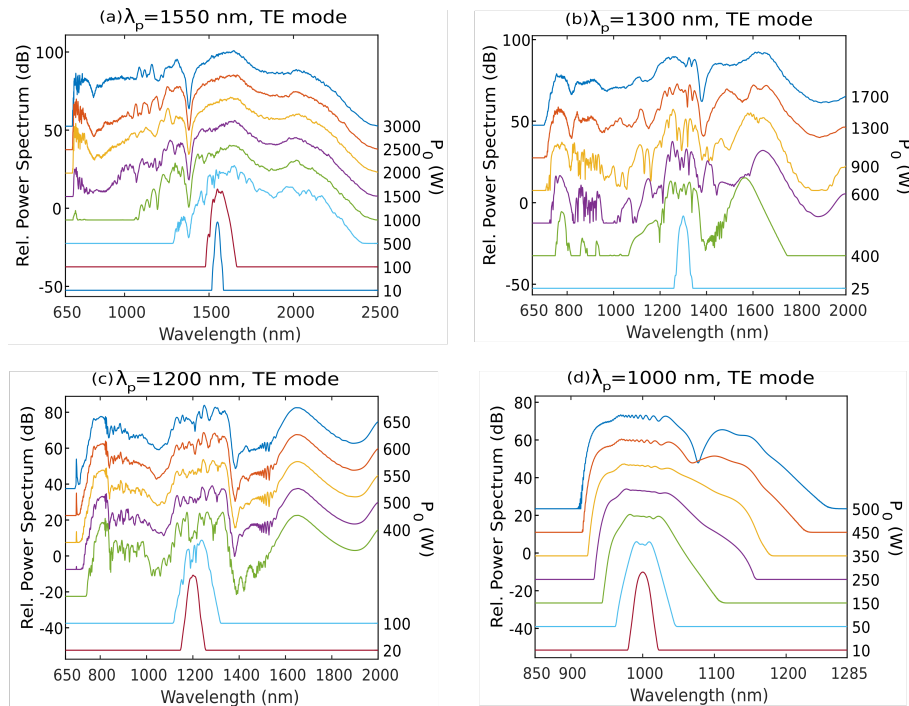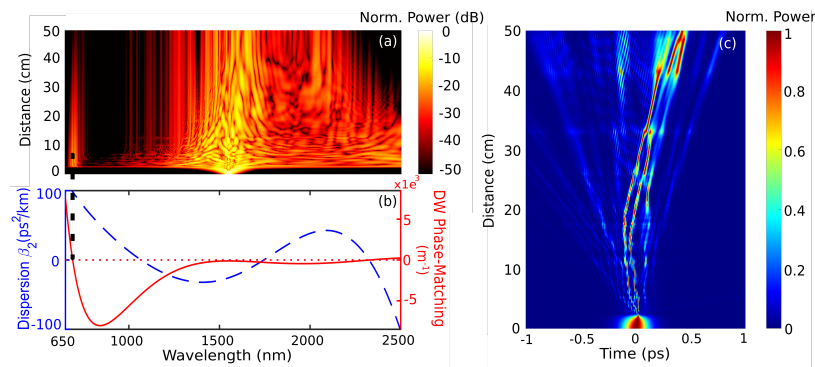

Fig. 9. Numerical simulations: SC spectra for different input peak powers P_0 shown on the right side of the graph and for different pumping wavelengths λ_P as those used experimentally. Simulations are based on the TE mode dispersion shown in blue in Fig.2(a).

Furthermore, when pumping at 1000 nm, we observe consistent behaviors between simulations and experiments (Fig. 6), particularly the symmetry in the spectra, which breaks upon reaching the first zero-dispersion wavelength (ZDW1) (Fig. 9(d)). An important aspect of the agreement between experiments and TE simulations is that the measurements were predominantly conducted along one of the TE/TM axes. This alignment is justified by the selection of the polarization angle, which aimed to maximize the spectral broadening, noting that SCs generated in the fundamental TM mode exhibited nearly identical characteristics to those in the fundamental TE mode. Nevertheless, a slight difference between experiments and simulations is noticeable, primarily attributed to wavelength-dependent losses (which were not fully characterized except at the telecom wavelength of 1550 nm, i.e. 0.1 dB/cm), but also due to variations in the responses and sensitivities of the two optical spectrum analyzers (OSAs). In terms of pumping power, the mean input powers used experimentally for SC generation agree well with the peak power considered numerically. For instance, when pumping at 1550 nm, a mean power of 200 mW corresponds to a peak power of 2 kW (i.e. pulse energy of 40 nJ), when coupling losses into the waveguide's core are taken into account.

To gain further insight into the physics of SC generation, we have plotted the SC spectro-temporal evolution dynamics in Fig. 10 when considering a pump wavelength of 1550 nm and a peak power of 1.5 kW, which corresponds to the purple spectrum shown in Fig. 9(a). As seen in Figs. 10(c), the pulse is progressively compressed at the onset of propagation so that, after only a few centimeters of propagation, solitons are ejected from the input pulse, and dispersive waves are generated. At this stage (i.e. around 3 cm of propagation), spectral broadening already reached its full extent, as typically observed experimentally in Fig. 7. To analyze DW generation, we calculated the phase-matching condition from the following equation [34]:

$$\beta(\omega_{DW}) - \beta(\omega_S) - \beta_1(\omega_{DW} - \omega_S) - \gamma P_S/2 = 0, \tag{2}$$

with ω_{DW} and ω_S representing the DW and soliton angular frequencies, respectively, and with β_1 being the inverse of the group velocity at the ω_S. The phase-matching is depicted as a red curve on the left of Fig. 10(b). As observed, phase-matching for the generation of a DW occurs at 710 nm, in good agreement with experimental observations.


Fig. 10. Numerical results: (a): SC spectral broadening dynamics along propagation distance in the 50-cm long integrated waveguide. Numerical simulations are obtained considering a peak power of 1.5 kW at 1550 nm; (b): Dispersion curve (blue, left) and dispersive wave phase matching (red, right) as a function of wavelength. (c): Corresponding temporal evolution dynamics of the SC along propagation in the waveguide.

9. SC coherence and noise

There are two main metrics used to analyze the SC noise properties: the first-order spectral coherence function and the relative intensity noise (RIN). We first modeled the SC coherence using the mutual coherence function, which can be written in the following form [2]:

$$|g_{12}(\omega)| = \left| \frac{\left\langle \tilde{A}_i^*(\omega)\tilde{A}_j(\omega) \right\rangle_{i \neq j}}{\sqrt{\left\langle \left| \tilde{A}_i(\omega) \right|^2 \right\rangle \left\langle \left| \tilde{A}_j(\omega) \right|^2 \right\rangle}} \right|,$$ (3)

where $A_i(\omega), A_j(\omega)$ represent independent pairs of complex spectral amplitude, and angle brackets indicate an ensemble average over independent SC pairs generated from N simulations with different noise seeds. In our simulations, we considered two noise sources including the quantum noise and the relative intensity noise (RIN) of the pump laser (1%), as in Ref. [35]. Simulation results are shown in Figs. 11 and 12 for two pump wavelengths at 1000 nm and 1550 nm in the ND and AD regimes, respectively. Specifically, we investigated the broadening and coherence in the TE (Fig. 11) and TM (Fig. 12) modes for different input peak powers. While SC coherence is well preserved in the ND pumping regime at 1000 nm for both TE/TM modes, as shown in Figs. 11(a) and 12(a), coherence is rapidly lost when pumping in the AD regime even at low peak power. This coherence loss is here mainly due to noise amplification processes such as modulation instability and Raman scattering. However, Fig. 12(b) shows that the coherence is fairly well preserved when pumping on the TM mode.
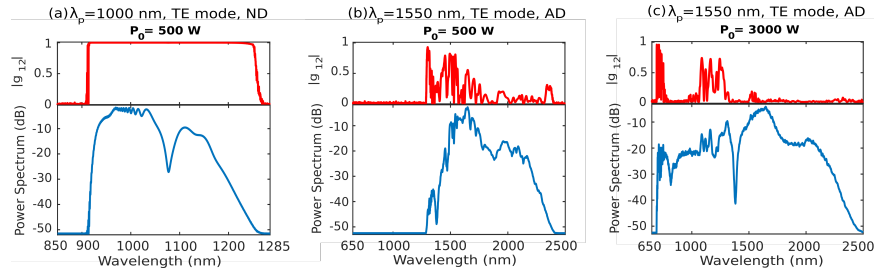

Fig. 11. Numerical simulations of SC generation (blue) and mutual coherence (red) at 1000 nm and 1550 nm, respectively, for the TE mode and different peak powers.
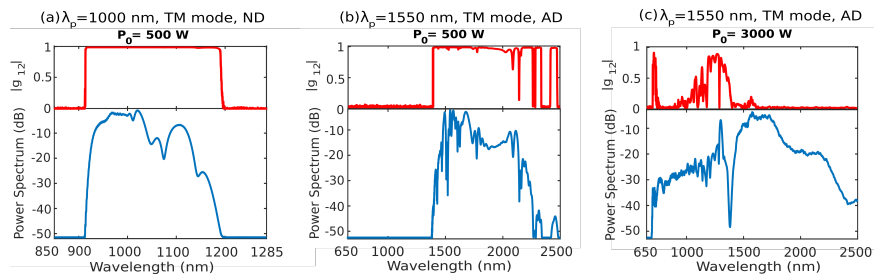
Fig. 12. Numerical simulations of SC generation (blue) and the mutual coherence (red) at 1000 nm and 1550 nm, respectively, for the TM mode and different peak powers.

We also conducted SC stability analysis using the DFT technique, as described in Fig. 4. This method allows for the direct recording of real-time, pulse-to-pulse SC spectra in the time domain

via DFT [25]. Specifically, to stretch the SC pulses, we added a 170-meter-long (normally dispersive) DCF at the chip's output fiber pigtail and then recorded the 80 MHz stretched pulse train using a high-speed photodiode (50 GHz) paired with a 20 GHz real-time oscilloscope. Due to the photodiode's predominant responsivity from 1400 nm to 1750 nm, we confined the SC real-time analysis within this spectral range while pumping the QXP chip waveguide at 1550 nm. The DCF fiber dispersion and slope are β_2=124 ps^2/km and β_3=2.7 ps^3/km, respectively. This gives an equivalent spectral resolution close to 5 nm. The results of DFT are shown in Fig. 13 for 1024 pulses, where the pulse-to-pulse spectra are displayed in gray and the corresponding average DFT spectrum (red line) is compared to the OSA spectrum (blue line). Although the SC does not appear to be fully broadened due to the limited detection bandwidth, the DFT average spectrum fits well with the OSA measurement over a dynamic range exceeding 20 dB.
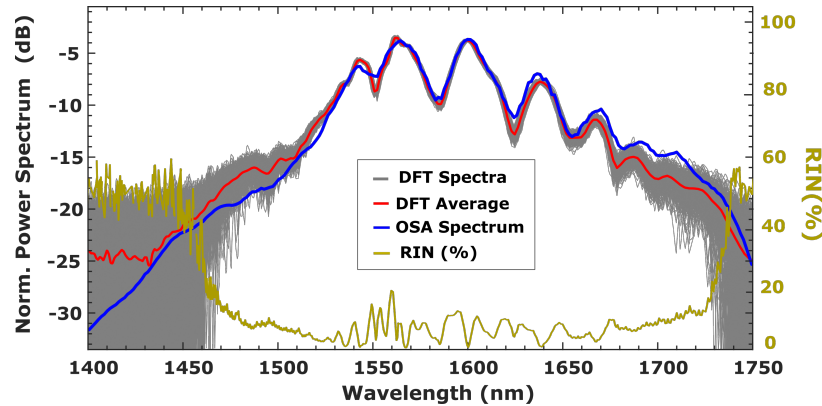
Fig. 13. Real-time pulse-to-pulse spectral measurements using DFT over 1024 pulses for a pump wavelength at 1550 nm and an input power of 256 mW. DFT pulse-to-pulse spectra (light gray), DFT averaged spectrum (red), OSA spectrum (blue), and RIN retrieved from DFT measurements (RIN, yellow).

Additionally, the DFT technique enables the straightforward measurement of spectral RIN, a crucial parameter for SC applications. Unlike the first-order spectral coherence function, the RIN formula only considers the SC intensity fluctuations without taking into account the effects of phase fluctuations. However, the RIN is a relevant metric to assess the overall SC stability, as it is described as the ratio between the standard deviation of the SC ensemble divided by its mean, as given in the following equation [31]:

$$\text{RIN}(\omega) = \frac{\sqrt{\left\langle \left(|\tilde{A}_i(\omega)|^2 - \left\langle |\tilde{A}_i(\omega)|^2 \right\rangle \right)^2 \right\rangle}}{\left\langle |\tilde{A}_i(\omega)|^2 \right\rangle}. \tag{4}$$

In our case, the RIN was measured from the pulse-to-pulse spectral fluctuations obtained via DFT and further reported, in yellow, in Fig. 13. Over the spectral range spanning from 1500 nm to 1700 nm, we found an average RIN as low as 7 %. The results also show that the RIN increases drastically on the SC edges due to both the reduction of the SC power and the detrimental impact of pump laser RIN on the output SC stability. The chip-based SC average RIN is relatively low, particularly considering the anomalous dispersion pumping regime, and it compares favorably with the state-of-the-art in optical fibers (5%) [30]. However, there is potential to further reduce the RIN by utilizing all-normal dispersion (ANDi) integrated optical waveguides. This could be achieved by optimizing the waveguide size to achieve all-normal flat dispersion, as demonstrated

with ANDi photonic crystal fibers, which can reduce the RIN to well below 1% [9]. Achieving low RIN and high coherence is essential for supercontinuum applications in optical sensing, imaging, and metrology.

10. Conclusion

In conclusion, this study explored supercontinuum (SC) generation in highly doped silica glass integrated waveguides of varying lengths (3 cm and 50 cm) under different dispersion regimes and input polarization angles. The broadest SC spectrum, spanning 700 nm to 2400 nm, was achieved with pumping at 1550 nm, while flatter SC spectra were observed when pumped at 1200 nm and 1300 nm. Additionally, greater stability in SC generation was demonstrated when pumping at 1000 nm within the normal dispersion regime. Notably, SC generation at 1550 nm was highly sensitive to input polarization, whereas this sensitivity was significantly reduced at shorter pump wavelengths.

Spontaneous Raman measurements of the high-index doped silica waveguides provided crucial data for enhancing the accuracy of numerical models. Coherence and noise analysis further revealed low relative intensity noise (RIN) across the SC bandwidth, highlighting the stability of the generated spectra.

These QXP glass-based integrated photonic waveguides exhibit excellent nonlinear optical properties, a straightforward manufacturing process, and seamless compatibility with fiber optic technologies. They hold significant promise for the development of compact, low-footprint, and low-pulse-energy SC sources powered by femtosecond fiber or chip-based integrated lasers. Such on-chip SC sources offer wide-ranging applications in fields requiring broad spectral coverage, including spectroscopy, telecommunications, and biomedical imaging, among others.

Data availability. Data underlying the results presented in this paper are not publicly available at this time but may be obtained from the authors upon reasonable request.

References

1. R. R. Alfano, *The Supercontinuum Laser Source: The Ultimate White Light* (Springer Nature, 2023).
2. J. M. Dudley and J. R. Taylor, *Supercontinuum Generation in Optical Fibers* (Cambridge University Press, 2010).
3. I. Zorin, R. Su, A. Prylepa, *et al.*, "Mid-infrared Fourier-domain optical coherence tomography with a pyroelectric linear array," Opt. Express **26**(25), 33428–33439 (2018).
4. C. Petersen, U. Møller, I. Kubat, *et al.*, "Mid-infrared supercontinuum covering the 1.4-13.3 μm molecular fingerprint region using ultra-high na chalcogenide step-index fibre," Nat. Photonics **8**(11), 830–834 (2014).
5. A. Manninen, T. Kääriäinen, T. Parviainen, *et al.*, "Long distance active hyperspectral sensing using high-power near-infrared supercontinuum light source," Opt. Express **22**(6), 7172–7177 (2014).
6. C. Poudel and C. F. Kaminski, "Supercontinuum radiation in fluorescence microscopy and biomedical imaging applications," J. Opt. Soc. Am. B **36**(2), A139–A153 (2019).
7. T. Udem, R. Holzwarth, and T. Haensch, "Optical frequency metrology," Nature **416**(6877), 233–237 (2002).
8. E. S. Lamb, D. R. Carlson, D. D. Hickstein, *et al.*, "Optical-frequency measurements with a Kerr microcomb and photonic-chip supercontinuum," Phys. Rev. Appl. **9**(2), 024030 (2018).
9. T. Sylvestre, E. Genier, A. N. Ghosh, *et al.*, "Recent advances in supercontinuum generation in specialty optical fibers," J. Opt. Soc. Am. B **38**(12), F90–F103 (2021).
10. D. Y. Oh, D. Sell, H. Lee, *et al.*, "Supercontinuum generation in an on-chip silica waveguide," Opt. Lett. **39**(4), 1046–1048 (2014).

11. D. Duchesne, M. Peccianti, M. R. E. Lamont, *et al.*, "Supercontinuum generation in a high index doped silica glass spiral waveguide," Opt. Express **18**(2), 923–930 (2010).
12. N. Singh, M. Xin, D. Vermeulen, *et al.*, "Octave-spanning coherent supercontinuum generation in silicon on insulator from 1.06 μm to beyond 2.4 μm," Light: Sci. Appl. **7**(1), 17131 (2018).
13. R. Halir, Y. Okawachi, J. S. Levy, *et al.*, "Ultrabroadband supercontinuum generation in a CMOS-compatible platform," Opt. Lett. **37**(10), 1685–1687 (2012).
14. A. R. Johnson, A. S. Mayer, A. Klenner, *et al.*, "Octave-spanning coherent supercontinuum generation in a silicon nitride waveguide," Opt. Lett. **40**(21), 5117–5120 (2015).
15. C. Lafforgue, S. Guerber, J. M. Ramírez, *et al.*, "Broadband supercontinuum generation in nitrogen-rich silicon nitride waveguides using a 300 mm industrial platform," Photonics Res. **8**(3), 352 (2020).
16. M. Sinobad, C. Monat, B. Luther-Davies, *et al.*, "Mid-infrared octave spanning supercontinuum generation to 8.5 μm in silicon-germanium waveguides," Optica **5**(4), 360 (2018).
17. M. Montesinos-Ballester, C. Lafforgue, J. Frigerio, *et al.*, "On-Chip Mid-Infrared Supercontinuum Generation from 3 to 13 μm Wavelength," ACS Photonics **7**(12), 3423–3429 (2020).
18. K. Hammani, L. Markey, M. Lamy, *et al.*, "Octave spanning supercontinuum in titanium dioxide waveguides," Appl. Sci. **8**(4), 543 (2018).
19. M. R. Lamont, B. Luther-Davies, D.-Y. Choi, *et al.*, "Supercontinuum generation in dispersion engineered highly nonlinear (γ = 10 /w/m) As_2S_3 chalcogenide planar waveguide," Opt. Express **16**(19), 14938–14944 (2008).
20. K. F. Fiaboe, A. D. Torre, A. Mitchell, *et al.*, "Design of Mid-Infrared Supercontinuum Generation in a strip-loaded LNOI Waveguide through lateral leakage engineering," in *European Conference on Integrated Optics*, (Enschede, Netherlands, 2023).
21. C. Li, X. Ren, H. Wu, *et al.*, "Octave-spanning visible supercontinuum generation from an aluminum nitride single crystal pumped by a 355 nm nanosecond pulse," Chin. Opt. Lett. **16**(4), 043201 (2018).
22. G. Granger, M. Bailly, H. Delahaye, *et al.*, "Gaas-chip-based mid-infrared supercontinuum generation," Light: Sci. Appl. **12**(1), 252 (2023).
23. C.-S. Brès, A. D. Torre, D. Grassani, *et al.*, "Supercontinuum in integrated photonics: generation, applications, challenges, and perspectives," Nanophotonics **12**(7), 1199–1244 (2023).
24. D. Moss, R. Morandotti, A. Gaeta, *et al.*, "New CMOS-compatible platforms based on silicon nitride and hydex for nonlinear optics," Nat. Photonics **7**(8), 597–607 (2013).
25. T. Godin, L. Sader, A. K. Kashi, *et al.*, "Recent advances on time-stretch dispersive fourier transform and its applications," Adv. Phys.: X **7**, 2067487 (2022).
26. M. Zerbib, V. Hoang, J. Beugnot, *et al.*, "Observation of Brillouin scattering in a high-index doped silica chip waveguide," Results Phys. **52**, 106830 (2023).
27. J. Z. Jiang, K. Stahl, R. W. Berg, *et al.*, "Structural characterization of cubic silicon nitride," Europhys. Lett. **51**(1), 62–67 (2000).
28. K. Goda and B. Jalali, "Dispersive Fourier transformation for fast continuous single-shot measurements," Nat. Photonics **7**(2), 102–112 (2013).
29. B. Wetzel, A. Stefani, L. Larger, *et al.*, "Real-time full bandwidth measurement of spectral noise in supercontinuum generation," Sci. Rep. **2**(1), 882 (2012).
30. R. D. S. Shreesha, T. Karpate, A. N. Ghosh, *et al.*, "Noise in supercontinuum generated using pm and non-pm tellurite glass all-normal dispersion fibers," Opt. Lett. **47**(10), 2550–2553 (2022).
31. E. Genier, S. Grelet, R. D. Engelsholm, *et al.*, "Ultra-flat, low-noise, and linearly polarized fiber supercontinuum source covering 670–1390 nm," Opt. Lett. **46**(8), 1820–1823 (2021).
32. K. E. Webb, Y. Q. Xu, M. Erkintalo, *et al.*, "Generalized dispersive wave emission in nonlinear fiber optics," Opt. Lett. **38**(2), 151–153 (2013).
33. G. Li, Y. Li, F. Ye, *et al.*, "Supercontinuum Generation in Dispersion Engineered Highly Doped Silica Glass Waveguides," Laser Photonics Rev. **17**(11), 2200754 (2023).
34. G. P. Agrawal, *Nonlinear Fiber Optics, fifth edition* (Elsevier & Academic Press, 2013).
35. E. Genier, P. Bowen, T. Sylvestre, *et al.*, "Amplitude noise and coherence degradation of femtosecond supercontinuum generation in all-normal-dispersion fibers," J. Opt. Soc. Am. B **36**(2), A161–A167 (2019).